Duality in the Mechanism of Hexagonal ZnO/Cu$_X$O Nanowires Inducing Sulfamethazine Degradation under Solar or Visible Light

Jiajie Yu [1,2], John Kiwi [1], Tianhe Wang [2], Cesar Pulgarin [1] and Sami Rtimi [1,*]

[1] Ecole Polytechnique Fédérale de Lausanne, EPFL-SB-ISIC-GPAO, Station 6, 1015 Lausanne, Switzerland; jiajie.yu@epfl.ch (J.Y.); john.kiwi@epfl.ch (J.K.); cesar.pulgarin@epfl.ch (C.P.)
[2] Chemicobiology and Functional Materials Institute, Nanjing University of Science and Technology, Nanjing 210094, China; thwang56@126.com
* Correspondence: sami.rtimi@epfl.ch

check for updates

Abstract: This study presents the first evidence for the photocatalytic performance of ZnO/Cu$_X$O hexagonal nanowires leading to sulfamethazine (SMT) degradation. The chemical composition of the nanowires was determined by X-ray fluorescence (XRF). The sample with the composition ZnO/Cu$_{x=1.25}$O led to faster SMT-degradation kinetics. The SMT-degradation kinetics were monitored by high performance liquid chromatography (HPLC). The morphology of the hexagonal nanowires was determined by scanning electron microscopy (SEM) and mapped by EDX. The redox reactions during SMT degradation were followed by X-ray photoelectron spectroscopy (XPS). The interfacial potential between the catalyst surface and SMT was followed in situ under solar and indoor visible light irradiation. SMT-degradation was mediated by reactive oxidative species (ROS). The interfacial charge transfer (IFCT) between ZnO and Cu$_X$O is shown to depend on the type of light used (solar or visible light). This later process was found to be iso-energetic due to the potential energy positions of ZnO and Cu$_X$O conduction bands (cb). The intervention of surface plasmon resonance (LSPR) species in the SMT degradation is discussed.

Keywords: metal-oxide nanowires; photocatalysis; sulfamethazine degradation; interfacial charge transfer; surface plasmon resonance

1. Introduction

Sulfamethazine (SMT) is one of the most important members in the family of sulfonamide antimicrobials and has been widely used in pharmaceuticals to protect animals against bacterial infections [1–4]. SMT is a persistent non-biodegradable environmental pollutant [5,6]. Residual SMT is excreted by animals to the surroundings and found in soils, food crops and drinking water [7–10], posing a threat to human health and the ecological system [11].

Several methods have been developed to remove SMT such as adsorption [12–14], biodegradation [15–17], advanced oxidation processes (AOPs) [18–22], and photocatalytic degradation [23,24]. It has also been reported that SMT is not completely eliminated by adsorption. Biodegradation by active sludge [15], Microbacterium sp. [16] and Achromobacter denitrificans PR1 [17] is possible, but requires long time periods and is restricted to low concentrations of SMT. Advanced oxidation processes (AOPs) such as Fenton and Fenton-like [18], photo-Fenton [19], electro-Fenton [20], ozonation [21], and gamma irradiation [22] have been reported to lead to SMT degradation. However, they need a high reagent concentration. Photocatalytic degradation of SMT mediated by Bi$_2$MoO$_6$ was recently reported by C. Guo et al., [23] with AgI/Bi$_{12}$O$_{17}$Cl$_2$ s in aqueous solution [24]. The present

study reports novel a semiconductor-oxide nanowire leading to SMT degradation. This study describes the catalyst preparation, the SMT degradation kinetics and the nanowire surface properties. A reaction mechanism is suggested based on the experimental data found during the course of this work.

ZnO is a widely studied photocatalyst for environmental remediation. Some recent reviews reflect the interest of ZnO in the field of applied photochemistry [25]. The solar light utilization of ZnO is limited due to the low absorption in the visible region < 4–5%. By coupling ZnO with oxide semiconductors with Cu_xO, the light absorption of the double-oxide reaches 800 nm [25]. Catalysts presenting optical absorption into the visible region for environmental applications is a subject of topical interest [26,27]. Depending on nanoparticle size and the preparation, ZnO presents a conduction band (cb) at 0.1–0.2 V (SHE) and a valence band (vb) positioned at ~3.4 (SHE) [28]. Cu–oxide has been chosen to decorate the ZnO to extend its spectral absorption into the visible range. For this objective, low amounts of Cu–oxide are needed compared to Mn and Fe [25] doping of ZnO. The use of Cu_xO is also an alternative to the addition of Ag and Pt to ZnO. This avoids the use of higher cost noble metals. ZnO is an inexpensive semiconductor widely used in the electronic industry due to its high electrical conductivity. At pH 1, the ZnO band gap (bg) is 3.2–3.4 eV depending on the preparation route used.

The notation Cu_xO is used for Cu–oxide since two oxidation states are present: CuO and Cu_2O. CuO presents typically a band gap of 1.7 eV and a conduction band at −0.4 V, and Cu_2O a band gap of 2.2 eV and a conduction band of −0.20 or −0.25 V [29]. Both Cu–oxides present visible light absorption [30,31].

This study presents the preparation of ZnO/Cu_xO hexagonal nanowires enhancing the SMT degradation with respect to bare ZnO. Evidence for two different interfacial charge transfer (IFCT) mechanisms between Cu_xO and ZnO under solar or visible light are reported. The use of TiO_2/Cu_xO leading to SMT degradation has been recently reported by our laboratory [32]. A dual mechanism was found to lead to SMT degradation under visible or sunlight irradiation. The surface properties of the ZnO/Cu_xO nanowires are reported in this study.

2. Results and Discussion

2.1. Description of the ZnO/CuxO (5%) Surface by Physical Methods

Figure 1 shows the images and morphology of the optimized ZnO/$Cu_{x=1.25}$O nanowire samples. Figure 1a shows the hexagonal nanowires with a media diameter of 1 to 2 microns and a length of 6–8 μm. The image was referenced in a 2 micron scale. Figure 1b shows the SEM imaging of ZnO/$Cu_{x=1.25}$O nanowires in a 2 micron scale. The arrows in Figure 1b indicate the presence of Cu_xO NPs that tend to aggregate. Using imageJ software, the particles size distribution of Cu_xO–NPs is in the range 18 to 28 nm as presented in Figure 1c. The values presented are the average of two distinct measurements (two big aggregates were left aside). Figure 1d–f show the EDX mapping of Zn, O and Cu, respectively.

(a)

(b)

(c)

Zn Lα1_2

(d)

O Kα1

(e)

Cu Lα1_2

(f)
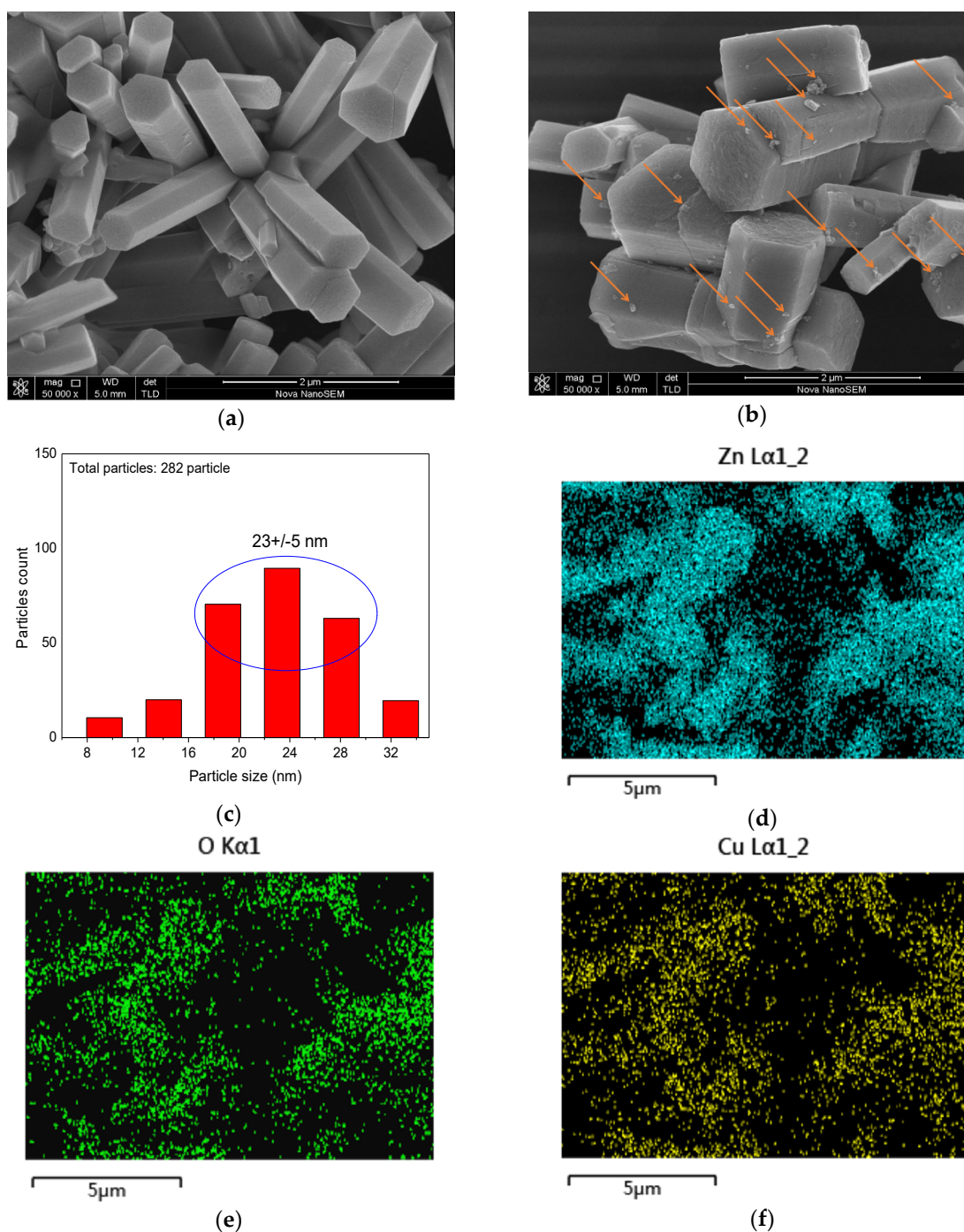
Figure 1. Scanning electron microscopy (SEM) imaging of ZnO and ZnO/$Cu_{x=1.25}O$ samples: (**a**) image of the hexagonal ZnO nanowires in a 2 micron scale, (**b**) image of the ZnO/$Cu_{x=1.25}O$ showing the Cu_xO NPs, and (**c**) size distribution of Cu_xO NPs using imageJ. The mapping by electron dispersive spectroscopy (EDX) shows the atomic distribution of (**d**) Zn, (**e**) O and (**f**) Cu.

Cu nanoparticles contain plasmons with free moving electrons presenting a collective oscillation and generating a local electromagnetic field. This affects the electronic states of the surrounding molecules. The plasmons transfer their energy into the nanowire-activating regions away from the excitation spot. The optical activity of NPs is determined by the wavelength of the plasmon resonance. This is a function of the particle size, shape and surrounding environment [33]. Plasmon studies have been widely reported for silver, with a peak around 400 nm [34]. Cu is an abundant and low-cost material compared to noble metals presenting inter-band transitions between 350 nm and 600 nm [35]

with a plasmonic peak/doublet around 500 nm [36]. Figure 1 shows Cu–NPs of 25–45 nm decorating the ZnO nanowires. Light absorbers like STM interact with the plasmon nanowires. This probably involves electron tunneling between both oxides.

The XRD diffractogram of ZnO/Cu$_x$O (5%) is presented below in Figure 2. The XRD diffractogram shows a structure typical of wurtzite hexagonal high crystallinity ZnO (JCPDS card No.36-1451) [37] with lattice parameters of a = 0.325 nm and c = 0.521 nm. The peaks centered at 35.4°, 38.7° and 48.7° were assigned to CuO (JCPDS card No. 45-0937). The crystallite sizes for ZnO and CuO were estimated by means of the Scherrer equation from the strongest peak signal:

$$D = \frac{K\lambda}{\beta \cos \theta}$$

where *D* stands for the crystal size in nm, *K* is the shape factor which is usually fixed as 0.89, λ is the wavelength which is taken as 0.154 nm, β is the full width at half maximum for the prominent peak, and θ is the Bragg's diffraction angle in radians. The values found were 40.24 nm for ZnO and 22.18 nm nm for CuxO. In Figure 2, the characteristic peaks of ZnO and CuO overlap as the ZnO and CuO appear at the same positions in the diffractogram. The system could be estimated to consist of CuxO decorating the ZnO crystallites since ZnO is the major component and CuO is present at a very low concentration.
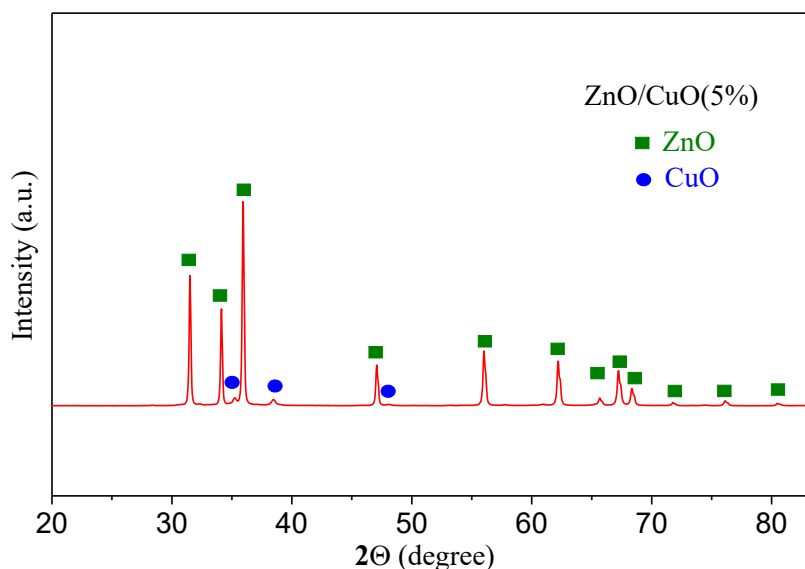

Figure 2. X-ray diffraction (XRD) pattern of ZnO/Cu$_{x=1.25}$O photocatalyst powder. For further details, see text.

2.2. Redox Catalysis and Interfacial Potential during SMT Degradation

The surface atomic concentration percentages and the change in Cu valence states in the ZnO/Cu$_x$O were determined by XPS. The results are shown in Figure 3a–d. No other elements besides Cu, O and Zn were detected except C. The latter element appears due to the sample exposure to air contamination. Figure 3b shows a shift for the Zn2p peaks from 1022.2 eV to 1021.6 eV during SMT photodegradation. This is evidence for the generation of Zn$^+$ species during SMT degradation. ZnO corrosion is due to the pH decrease produced by acids formation as intermediate species during SMT degradation (please see Figure 4). The observed reduction of Zn^{2+} to Zn$^+$ is similar to the reduction of TiO$_2$ to Ti^{3+} reported during the degradation of several pollutants [38]. This shows redox reactions occurring at the interface of ZnO nanowires during SMT degradation. The corrosion of ZnO is further confirmed by the data presented in Figure 4. The pH of the solution shifts from 7.2 to ~6.4 during the photocatalytic

degradation of SMT under solar-simulated light. This is due to ZnO corrosion at pH < 6.5. This last pH value depends on the make-up and chemical species present in the suspension.
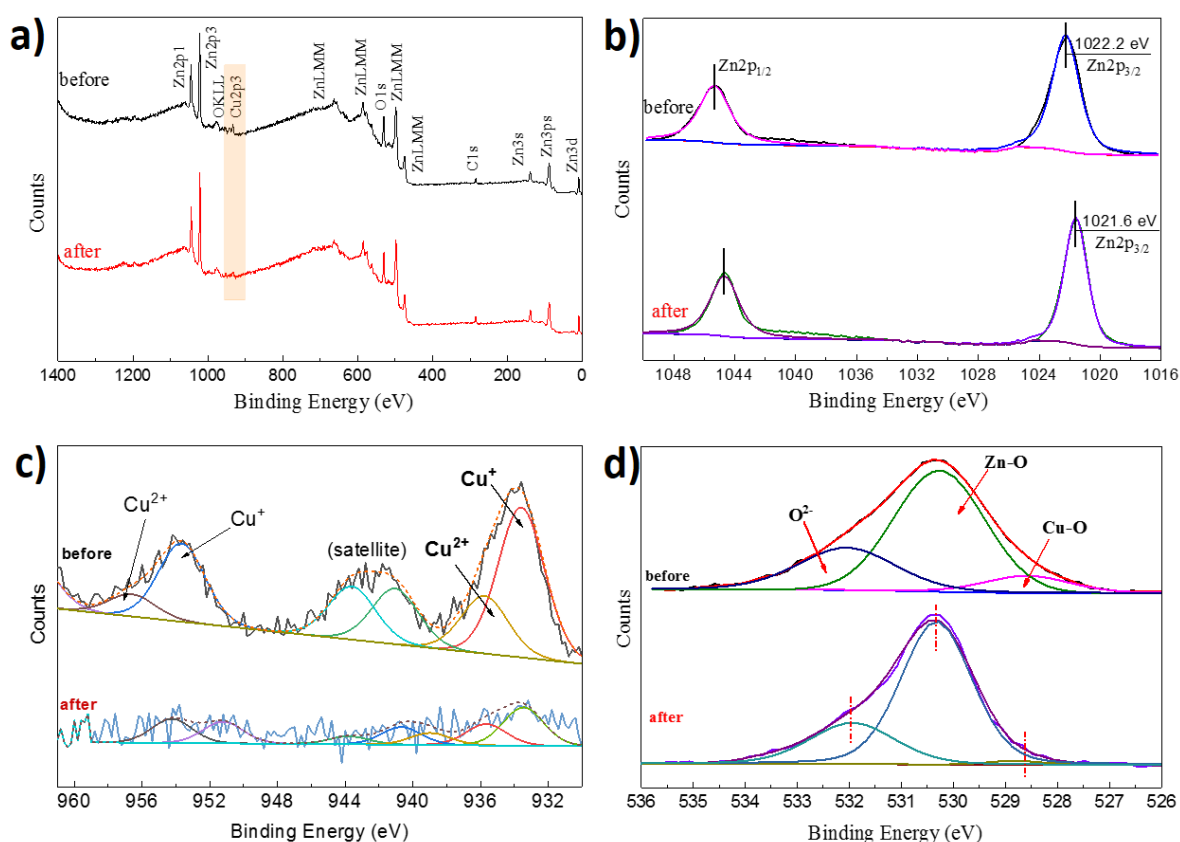
Figure 3. (**a**) X-ray photoelectron spectroscopy (XPS) survey spectra of ZnO/Cu$_{x=1.25}$O; (**b**) Zn2p peak shifts during SMT degradation; (**c**) Cu2p shifts during SMT degradation; and (**d**) O1s shift observed during SMT degradation.
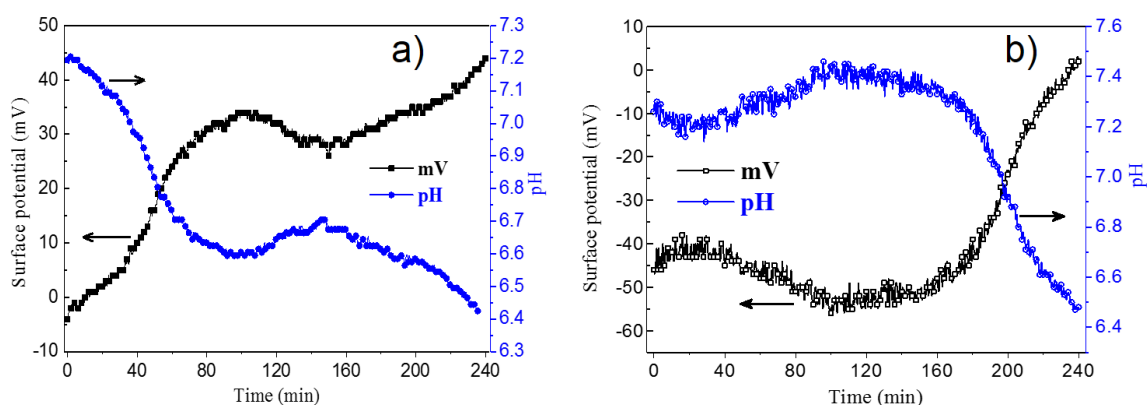
Figure 4. Surface potential and local pH of the ZnO/Cu$_{x=1.25}$O nanowires under: (**a**) simulated solar light and (**b**) visible light irradiation during SMT degradation. Solution parameters: [catalyst] = 500 mg/L, [SMT] = 2.5 mg/L and initial pH 7.0.

The BE peak shifts observed in the deconvolution of Cu2p illustrated in Figure 3c presents the evidence for redox reactions occurring during the SMT photocatalytic degradation. The peaks at 935.4 eV and 956.2 eV correspond to Cu^{2+}, with typical CuO. The satellite peaks appear at 941.2 eV and 943.4 [39–41]. XPS shows that Cu$_2$O oxide was the predominant Cu species on the ZnO/Cu$_{x=1.25}$O. After SMT degradation as shown in Figure 3c, the Cu$_2$O peak (net Cu$^+$) decreases. This occurs on

localized surface plasmon resonance (LSPR) present on the nanowire surface. The LSPR contribution to the SMT degradation will be further discussed in the section below. The surface atomic percentage of Cu in the ZnO/Cu$_{x=1.25}$O sample is seen to be 7.32% in Table 1.

Table 1. Surface atomic percentage concentration of the elements determined by X-ray photoelectron spectroscopy (XPS) in the ZnO/Cu$_{x=1.25}$O sample.

	C1s	N1s	O1s	Na1s	Cu2p	Zn2p
Before SMT degradation	13.78	0.00	42.58	0.00	7.32	36.32
After SMT degradation	14.02	0.00	41.99	0.00	6.92	37.06

The O1s deconvolution in Figure 3d shows the presence of three peaks located at 532.0 eV, 530.3 eV and 528.5 eV and assigned to the O^{2-} deficient regions of Zn–O and Cu–O [39,40]. Table 1 presents the atomic surface percentage concentration of the elements in the ZnO/Cu$_{x=1.25}$O sample before and after SMT degradation. The C1s percentage on the initial sample is due to C residues from the air and from the residual C in the solutions used to prepare the samples. The C content slightly increases after the SMT degradation due to the non-mineralized SMT species (see equation 1 below). The O1s and Cu2p percentage decrease due to the C1s being deposited on the sample during SMT degradation. The small increase in the Zn2p percentage observed after SMT degradation is due to the destruction of impurities present on the initial pristine ZnO by oxidative radical species (see below Section 3.4).

Figure 4a,b show the surface potential and local pH of the ZnO/Cu$_{x=1.25}$O nanowires under: (a) simulated solar light and (b) visible light irradiation. Figure 4a shows that the initial potential increases up to 170 min and increases again due to the presence of the SMT intermediates generated during the SMT degradation. Figure 5 shows that the SMT degradation reaches ~75% after 170 min (trace g). A similar pattern was seen for the surface potential variation in Figure 4b for the SMT degradation under visible light. In both cases, the initial potentials (Eigenvalues) were seen to be different. The changes in the interfacial potential during SMT photodegradation in Figure 4b present a trend similar to the one shown in Figure 4a. This suggests in both cases a similar mechanism.
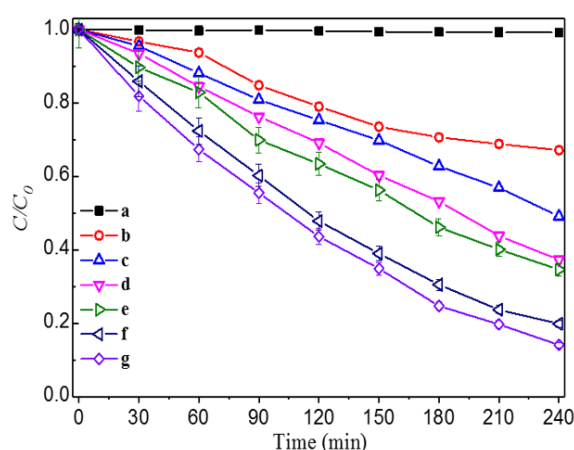
Figure 5. Degradation of sulfamethazine (SMT) on: (**a**) ZnO/Cu$_x$O (5%) in the dark, (**b**) Cu$_x$O, (**c**) ZnO/Cu$_x$O (1%), (**d**) ZnO, (**e**) ZnO/Cu$_x$O (2.5%), (**f**) ZnO/Cu$_x$O (10%), and (**g**) ZnO/Cu$_x$O (5%) under simulated solar light (310 nm–800 nm). Solution parameters: [catalyst] = 500 mg/L, [SMT] = 2.5 mg/L, initial pH 7.0, and solar light intensity 50.1 mW/cm^2.

The variation of the initial pH 7 during SMT degradation is shown in Figure 4a,b (right-hand axes). This variation was due to the organic acids (branched or not) generated during SMT degradation. Additional cationic species contribute to the pH drop as the degradation time progresses. The production

of organic acid intermediates was reported by Kraeutler and Bard [42] due to the photo-Kolbe reaction as shown in Equation (1) below

$$SMT + ZnO/Cu_xO \overset{solar/visble\ light}{\rightarrow} RCOO - + intermediate\ acids/cations + CO_2 \tag{1}$$
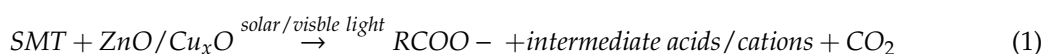
A pH decrease from 7.2 down to 6.4 was observed for the SMT degradation under solar light in Figure 4a,b. This is equivalent to an eight-fold increase in the concentrations of H^+ in the solution. Short-chain carboxylic acids (C_1–C_4) with pKa values around ~3.0 [38] are generated in the solution and account for the pH drop. The SMT follows the sequence: sulfanilic acid → benzoquinone → maleic/fumaric acid → acetic/oxalic/formic acid → CO_2 as reported in references [20–25]. The intermediate carboxylic acids are subsequently eliminated in the last step of the SMT degradation as CO_2. Supplementary Tables S1 and S2 provide the values for the pH decreases.

2.3. SMT-Degradation on ZnO/CuxO: Effect of Light Intensity

Figures 5 and 6 present the degradation of SMT on ZnO/CuO under solar-simulated and visible light irradiation in a solution with initial pH 7, respectively. The SMT degradation kinetics are slower for the sample ZnO/CuxO (10%) in Figure 6 (trace f) compared to the ZnO/CuO(5%) sample in (trace g). CuO doping has been reported to decrease the ZnO band gap.
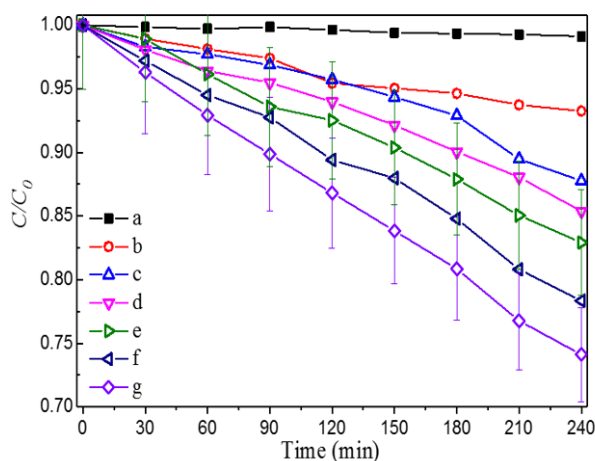
Figure 6. Degradation of sulfamethazine (SMT) on: (**a**) ZnO/Cu$_x$O (5%) in the dark, (**b**) Cu$_x$O, (**c**) ZnO/Cu$_x$O (1%), (**d**) ZnO, (**e**) ZnO/Cu$_x$O (2.5%), (**f**) ZnO/Cu$_x$O (10%), and (**g**) ZnO/CuO (5%) under visible light (> 410 nm). Solution parameters: [catalyst] = 500 mg/L, [SMT] = 2.5 mg/L, initial pH 7.0, and visible light intensity 38.9 mW/cm^2.

The effects of SMT and of ZnO/Cu$_x$O concentrations on the degradation kinetics are shown in the Supplementary Figures S1 and S2. The single HPLC peaks during the SMT degradation on ZnO/Cu$_{x=1.25}$O samples is shown in Figure 7.
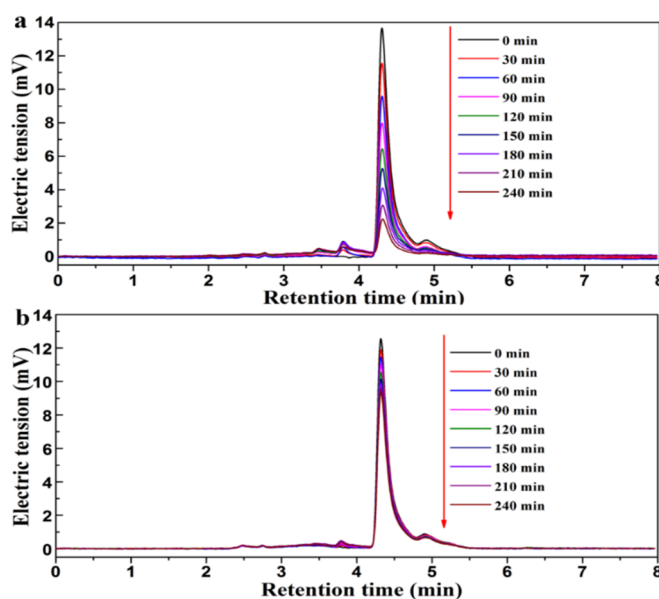
Figure 7. SMT degradation peaks obtained by high pressure liquid chromatography (HPLC) mediated by ZnO/Cu$_{x=1.25}$O %) nanowires under (**a**) simulated solar light irradiation and (**b**) visible light irradiation. Solution parameters: Solution parameters: [catalyst] = 500 mg/L, [SMT] = 2.5 mg/L, initial pH 7.0.

SMT presents two pKa values at 2.8 and 7.4 giving rise to SMT$^+$, SMT and SMT$^-$ species [43]. Sulfamethazine is a weak acid due to the strong electron attraction of the -SO$_2$ substituent and the resonance stabilization of the sulfamethazine anion [44]. SMT degradation runs at different pH values are reported in Supplementary Figure S4. Figure S4 shows that the fastest degradation takes place at pH values of 3. At pH 3, ZnO corrosion lead to the release of Zn^{2+}-ions in the solution since ZnO is stable at pH > 6.5. These Zn^{2+}-ions catalyze the SMT degradation via Fenton-like reactions [45,46].

The ZnO presents an isoelectric point (IEP) of ~9.3, and the value for CuO is ~9.5 [47]. The two oxides are positively charged at pH values ~7. The negatively-charged groups of SMT and the positive ZnO/CuO interface lead to an electrostatic interaction between both components. The SMT equilibria as a function of the solution pH is shown in Scheme 1. At pH 7, an SMT-zwitterion is present since this solution pH is positioned between pKa1 and pKa2.
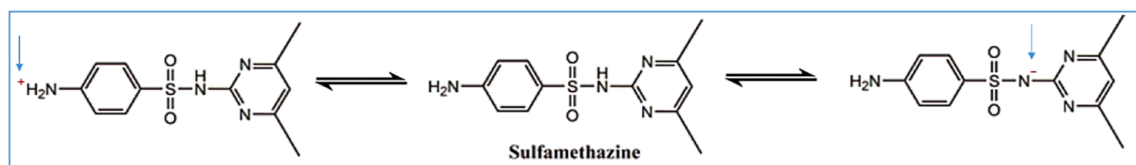
Scheme 1. SMT equilibria showing their negative, zwitterion and positively-charged functionalities as a function of the solution pH.

Figure 8 presents the effect of light intensity on the SMT degradation kinetics on ZnO/Cu$_{x=1.25}$O %) under solar light and visible light. The SMT degradation efficiency increased with the applied light intensity. This is evidence that the photocatalyst presents semiconductor behavior during SMT degradation under band-gap irradiation. A larger amount of photogenerated charges is generated by a semiconductor at higher light doses leading to a faster SMT degradation. This is shown in Figure 8a,b.
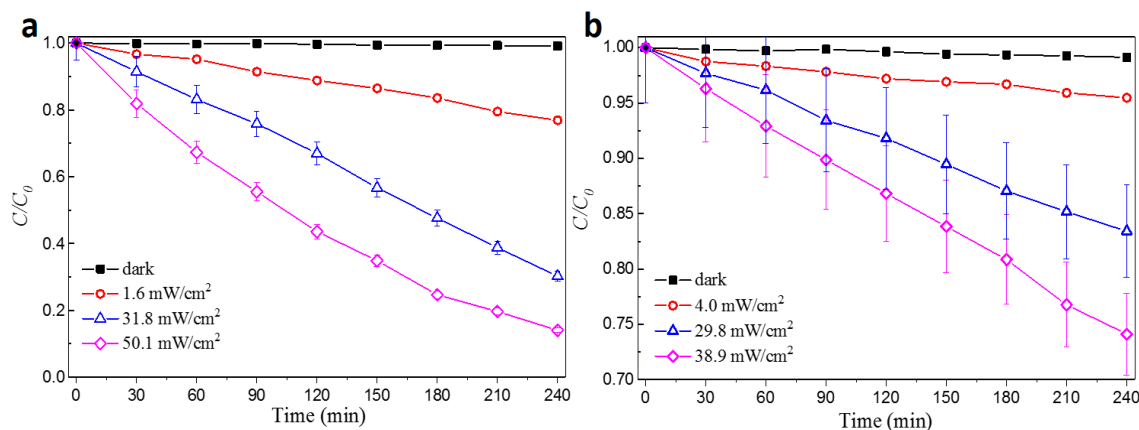
Figure 8. Effect of light intensity on the SMT degradation kinetics by ZnO/Cu$_{x=1.25}$O under (**a**) simulated solar light and (**b**) visible light. Solution parameters: [catalyst] = 500 mg/L, [SMT] = 2.5 mg/L and initial pH 7.0.

The optical absorption of Cu$_x$O occurs between 300 nm and 800 nm [42] and the SPR absorption peaks were reported at 390, 570, and 590 nm depending on the Cu$_x$O size [48,49]. When Cu_oxide is exposed to light, the conduction electrons in the nanoparticle oscillate coherently due to the electromagnetic field associated with the incoming light. The electric field associated with the incident light excites the Cu$_x$O upper electron shells. This increases the electron oscillations, inducing a Cu$_x$O electric field on the surface of the Cu$_x$O nanocrystals [50,51].

2.4. Determination of the ROS-Species during SMT-Degradation

To understand the photocatalytic mechanism of SMT degradation, the determination of the ROS species was carried using the appropriate radical scavengers: methanol ($^\bullet$OH scavenger); p-benzoquinone ($^\bullet$O$_2^-$ scavenger); NaN$_3$ (^{1}O$_2$ scavenger); and disodium ethylene-diamine-tetra-acetate dehydrate (EDTA-2Na), a hole scavenger. A scavenger concentration of 0.5 mM reagent was used in all cases. Figure 9 shows that the SMT degradation under visible light was decreased by 60% and 58% when EDTA-2Na and methanol were added to the solution. In this way, vbh$^+$ and $^\bullet$OH-radicals were found as the two main radicals leading to SMT degradation. The SMT degradation was reduced by 20% when benzoquinone as an HO$_2$/$^\bullet$O$_2^-$ scavenger was added to the solution. The unambiguous determination by NaN$_3$ of ^{1}O$_2$ and CH$_3$OH of $^\bullet$OH-radicals was not possible. NaN$_3$ also scavenges the $^\bullet$OH radicals. Possibly, ^{1}O$_2$ and $^\bullet$OH-radicals intervene jointly in SMT degradation. The $^\bullet$OH radical intervention ($^\bullet$OH/HO$^-$ −1.90–2.20 V vs NHE) [52] predominates, leading to SMT-oxidation. The ^{1}O$_2$/O$_2^-$ potential of +0.08V NHE [53] is much lower compared to the $^\bullet$OH/HO$^-$ reaction. The identification of ROS radicals followed the approach used in TiO$_2$ photocatalysis when investigating the ROS intervention, leading to pollutant degradation. However, ZnO/CuxO-mediated photocatalysis may not follow the pattern valid for TiO$_2$ photocatalysis [54]. Figure 10 shows the data for scavenging of ROS carried under visible light.
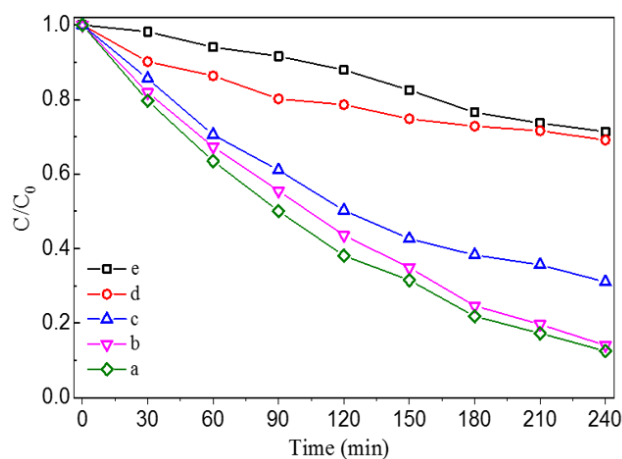
Figure 9. Intervention of ROS scavengers during SMT degradation by ZnO/Cu$_{x=1.25}$O %) under simulated solar light on the following: (**a**) 0.01 mM NaN$_3$, (**b**) no scavenger, (**c**) 0.5 mM p-benzoquinone, (**d**) 0.5 mM methanol, and (**e**) 0.5 mM EDTA-2Na. The light intensity under visible light irradiation was 50.1 mW/cm^2.
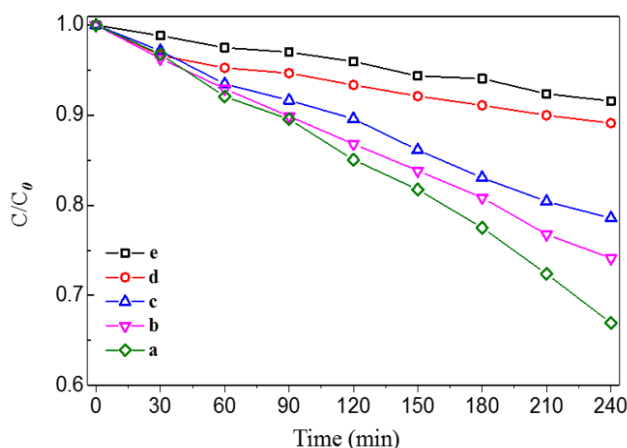
Figure 10. Intervention of ROS scavengers during SMT degradation by ZnO/Cu$_{x=1.25}$O %) under visible light on the following: (**a**) 0.01 mM NaN$_3$, (**b**) no scavenger, (**c**) 0.5 mM p-benzoquinone, (**d**) 0.5 mM EDTA-2Na, and (**e**) 0.01 mM methanol. Solution parameters: [catalyst] = 500 mg/L, [SMT] = 2.5 mg/L, initial pH 7.0. The light intensity under visible light irradiation was 38.9 mW/cm^2.

2.5. IFCT Mechanisms Suggested under Solar and Visible Light: Involvement of the LSPR

Figure 11a presents the IFCT for reactions photocatalyzed by ZnO/Cu$_{x=1.25}$O under low-intensity solar-simulated light. The ZnO in Figure 11a generates the holes leading to the SMT degradation [55]. During the IFCT, the ZnOvb transfers holes (h+) to the Cu$_x$Ovb, increasing the carrier lifetime. This partially hinders the charge-pair recombination in Cu$_x$Ovb.
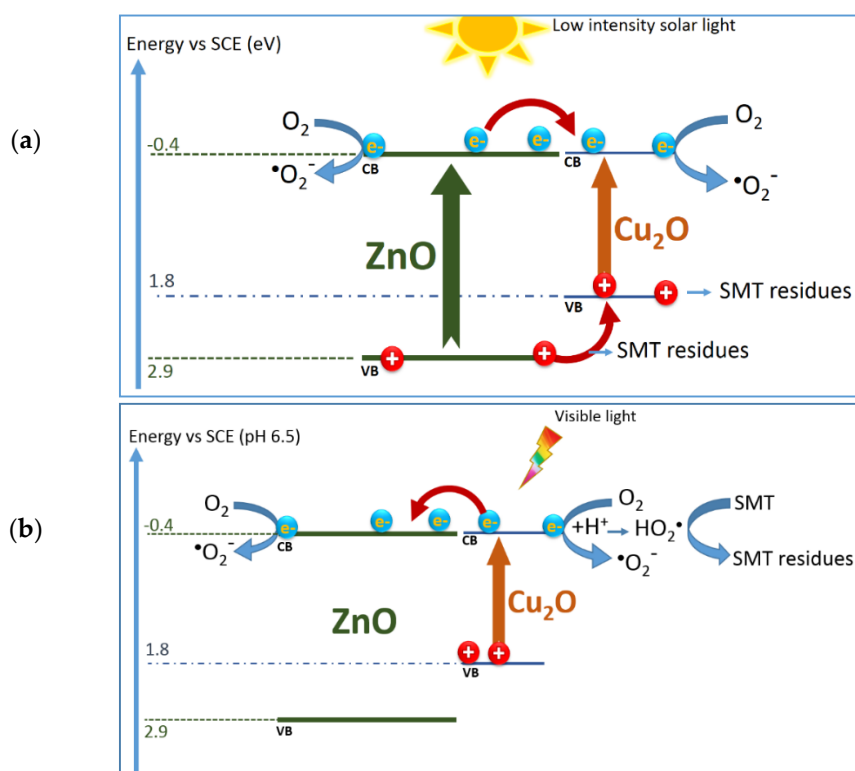
Figure 11. Suggested interfacial charge transfer mechanism (IFCT) during the SMT degradation on ZnO/$Cu_{x=1.25}O$ under (**a**) simulated solar light and (**b**) visible light at pH 6.5.
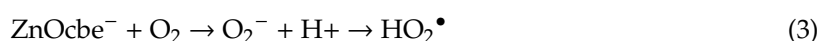
Figure 11b presents the visible light irradiation of the ZnO/CuO samples where Cu_xO absorbs the visible light > 410 nm. The absorber reacts by the build-up of surface plasmon resonance species (LSPR). In this case, charge recombination occurs on the Cu_xO surface due to: (a) the close proximity of the photo-generated charges on the Cu_xO surface facilitating the charge recombination and precluding charge diffusion to the non-absorbing ZnO component. The higher recombination rate limits the amount of free charges leading to SMT degradation. The SMT degradation under visible light irradiation does not involve reactions on the ZnO valence band (see Figure 11a)

Scheme 2 shows the SMT functional group coordination with ZnO and ZnO/CuO. Low potential (or sub-potential) photoinduces holes/mid-gap states in the ZnO/$Cu_{x=1.25}O$ samples. In the presence of SMT, these mid-gap holes would photo-induce $^1O_2$ through the oxidation of $O_2^{-\bullet}$ in a thermodynamically allowed reaction [29,42]. Photo-induced holes that have a lower oxidation potential would oxidize $O_2^{-\bullet}$ (+0.34 V vs NHE). The $O_2^{-\bullet}$ occurs due to the reduction of molecular oxygen by cb electrons as shown above in Figure 11. The oxidation of superoxide radicals (see Section 3.4) by photoinduced vb holes may also lead to the singlet oxygen/hydroxyl radicals ($^\bullet OH$) [52,53].
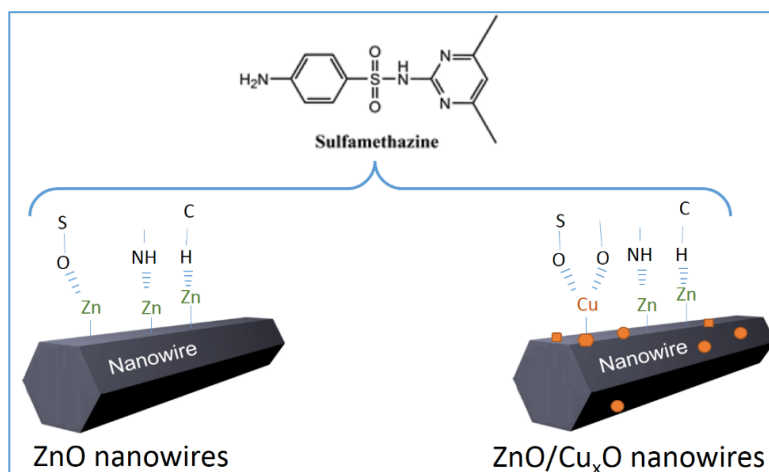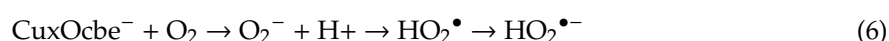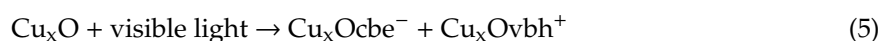
Scheme 2. Sulfamethazine functional group coordination with ZnO and ZnO/Cu_xO.

A mechanism for SMT degradation is suggested in Equations (2)–(7) as outlined in Figure 11a for SMT degradation under solar-simulated light:

$$ZnO/Cu_xO + solar\ light \rightarrow ZnOcbe^- + ZnOvbh^+ + CuOcbe^- + CuxOvbh^+ \tag{2}$$

$$ZnOcbe^- + O_2 \rightarrow O_2^- + H+ \rightarrow HO_2^\bullet \tag{3}$$

$$HO_2^\bullet + SMT \rightarrow CO_2 + H_2O,N,S \tag{4}$$

The crucial step under solar irradiation in Figure 11a is the electron injection from $ZnOcbe^-$ into the minority component Cu_xO in the ZnO/$Cu_{x=1.25}O$. The heterojunction between ZnO and Cu_xO has been reported [56,57] for the detection of H_2S [58] and for the monitoring of H_2 production [59]. Another mechanism to consider besides the one suggested in Equations (2)–(7) involves photosensitization of ZnO/$Cu_{x=1.25}O$ during SMT degradation. This would be more important during the initial stages of the STM degradation.

A mechanism for SMT degradation under visible light is suggested in Figure 11b as:

$$Cu_xO + visible\ light \rightarrow Cu_xOcbe^- + Cu_xOvbh^+ \tag{5}$$

$$CuxOcbe^- + O_2 \rightarrow O_2^- + H+ \rightarrow HO_2^\bullet \rightarrow HO_2^{\bullet-} \tag{6}$$

$$HO_2^\bullet + SMT \rightarrow CO_2 + H_2O,N,S \tag{7}$$

Different SMT degradation mechanisms are suggested for pollutants' degradation under solar or visible light as noted in Figure 11a,b.

The reduction of the Cu_2O shown in Figure 3 may proceed by two mechanisms: (i) radiative energy transfer from Cu-plasmon state to Cu_xO enhancing the electrons' transition from the bonding orbitals in the valence band to the anti-bonding orbitals in the conduction band. This would weaken the Cu–O bonding leading to Cu_2O reduction, and (ii) electronic states of ZnO or CuO excited by the type of light used interacting with Cu_xO LSPR. In the latter case, the electron injection can be direct or indirect depending on the Cu oxidation state during SMT degradation. The plasmons interact with the anti-bonding Cu_xO states. However, in the indirect process, Landau damping takes place involving plasmon decay and leading to hot electrons. These electrons are subsequently transferred to Cu_2O. Scheme 3 below suggests two LSPR mechanisms for ZnO/Cu_xO surface under light. Scheme 3 suggests the direct electron injection into Cu_xO during SMT degradation. This is favored by the increase in the dielectric function on the photocatalyst surface. Under solar light, the latter process may proceed faster compared to visible light illumination. Both mechanisms suggested above for the photocatalytic

degradation of SMT are not completely understood at the present time and more work is needed in this direction.
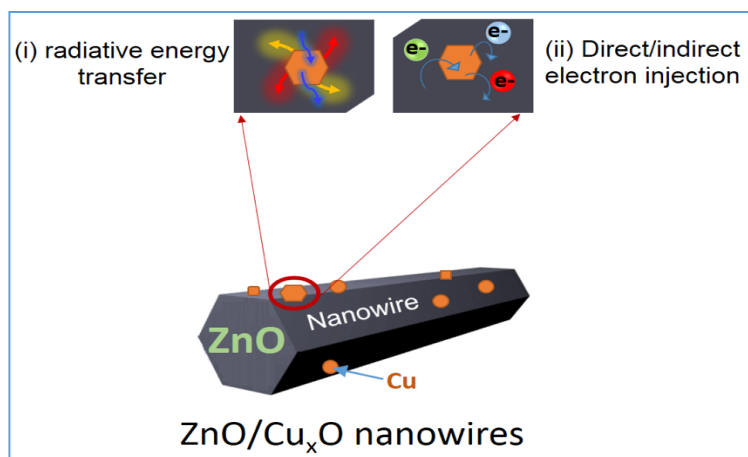
Scheme 3. Schematic illustration of the LSPR suggested at the interface of ZnO/Cu$_x$O nanowires.

3. Materials and Methods

3.1. Preparation of ZnO/Cu$_x$O Hexagonal Wurtzite Nanowires

The synthesis of ZnO hexagonal nanowires decorated with Cu$_x$O was carried out aiming at fast STM degradation [60]. A solution of 200 mL of 0.1 M zinc nitrate containing Cu(NO$_3$)$_2$ and 200 mL of 0.1 M hexa-methylene-tetramine (HMT) was mixed under stirring. This solution was transferred to a 500-mL flask and refluxed at 90 °C for 3 days. The final suspension was filtered, washed with de-ionized water and ethanol, and later oven-dried in air atmosphere. The resulting powders were calcined at 500 °C for 1 h with a heating rate of 5 °C/min. Calcination of ZnO/Cu$_x$O nanowires: In separate experiments, Cu$_x$O were prepared by heating a Cu(NO$_3$)$_2$ aqueous solution to dryness at 110 °C followed by calcination at 500 °C for 1h. A long series of experiments with various ZnO:CuO ratios were run to optimize the ratio of the ZnO to CuO leading to the fastest SMT photodegradation. The sample leading to the fastest SMT degradation was prepared by mixing solutions of ZnO and CuO in the ratio of 20:1. This ratio can also be formulated as ZnO/Cu$_x$O (5%).

3.2. Nanowires Properties Determined by Surface Physical Methods

The composition of the optimized photocatalyst ZnO/CuxO(5%) was determined by X-ray fluorescence (XRF) and found the present composition of ZnO/Cu$_{x=1.25}$O. The XRD unit used was an Oribs PC Micro EDXRF analyzer (Shanghai, China) with a Rh source (20 kV, 1 mA) and an Apollo XRF-ML50 Silicon Drift Detector (Shanghai, China) with an energy resolution lower than 135 eV at the MnKa. The elementary crystal sizes for ZnO and Cu$_x$O were estimated by the Scherrer equation from the strongest peak signal.

SEM imaging was carried out in a field-emission scanning electron microscopy (FESEM, Hitachi S4800, Shanghai, China) operated at 20 kV. The images were mapped by EDXS. Particle size distribution assessment of the Cu$_x$O NPs were carried out by means of Image J software 1.50i (Wayne Rasband, National Institutes of Health, Maryland, USA).

3.3. X-ray Photoelectron Spectroscopy and Interfacial "In Situ" Potentials Determination

The atomic surface concentration percentage and chemical state of Zn and Cu of the ZnO/Cu$_{x=1.25}$O were determined by X-ray photoelectron spectroscopy (XPS) in an AXIS NOVA X-ray photoelectron spectrometer from Kratos Analytical, Manchester, UK provided for with a monochromatic AlK (hν = 1486.6 eV) anode. The binding energies (BE) were calibrated against the standard C1s binding

energy at 284.8 eV. The spectra were deconvoluted by means of a Multipak (version 9 software) using 50:50 Gaussian-Laurentzian. Background subtraction correction was Shirley [61]. At this level, it is worth reminding the surface percentage calculation/estimation method. To estimate the surface atomic percentage of the elements of the peaks of interest, first, one should divide the intensity by the X-ray flux, then by the photoionization cross-section for the core level. This allows estimating the probability that a photoelectron will be emitted. This emission is different for each atomic core level at each photon energy. After normalizing these results, the ratio of the elemental percentages can be found.

The in situ interfacial potential during the SMT-degradation was monitored as a function of time in a pH/mV/Temp meter (Jenco 6230N, San Diego, USA) equipped with a microprocessor and a RS-232-C IBM interface.

3.4. Irradiation Procedures and ROS Analysis.

The photodegradation of SMT was carried out in the cavity of a Suntest solar simulator CPS (Atlas GmbH, Hanau, Germany). In a typical run, 25 mg of the selected photocatalyst was placed in a 50-mL photochemical reactor with 2.5 mg/L SMT. The pH of the pollutant solution was adjusted by 0.1 M NaOH or 0.1 M HCl solutions. Prior to irradiation, the samples were equilibrated in the dark for 30 min. At preselected times, 2 mL aliquots were withdrawn to evaluate the SMT degradation kinetics. For runs in the visible light range, a cut-off filter ($\lambda > 410$ nm) was inserted during the irradiation runs in the solar simulator.

The amount of SMT was determined by high performance liquid chromatography in an HPLC Agilent 1100 instrument (Waldbronn, Germany) equipped with a C18 column (Supercosil LC-18, 5 μm particle size, length 15 cm, id. 3mm) and a UV detector ($\lambda = 270$ nm). SMT aliquots of 20 μL were injected into the HPLC acetonitrile with 0.1% formic acid solution mobile phase (40:60) and a flow rate of 0.85 mL/min. The effect of the light intensity was monitored in the Suntest simulator by varying the applied power to the Xe-light source. Scavenging experiments were carried out to determine the reactive oxygen species (ROS) using: p-benzoquninone as the $HO_2^{\bullet-}$ radical scavenger, NaN_3 as the singlet oxygen $^1O_2$ scavenger, methanol as the $^{\bullet}$OH-radical scavenger and EDTA-2Na as the hole (vbh^+) scavenger [30].

The sulfamethazine structural formula is shown next in Scheme 4.
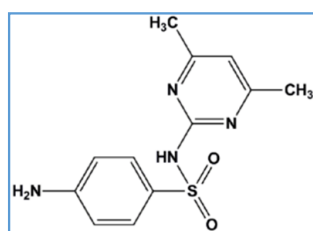
Scheme 4. Structural formula of sulfamethazine (SMT.).

The results deviation was estimated using the ANOVA statistical method. All the kinetic experiments reported in this study were carried out in triplicates.

4. Conclusions

Two mechanisms are suggested for ZnO/Cu_xO leading to SMT degradation under solar or visible light. The $ZnO/Cu_{x=1.25}O$ sample led to the fastest SMT degradation. CuO was the predominant form of the Cu–oxide species as detected by XPS. When Cu_xO is irradiated under visible light, the SMT degradation kinetics are slower compared to the kinetics attained under solar irradiation. The SEM/EDXS images for $ZnO/Cu_{x=1.25}O$ provide evidence for nanowires with a hexagonal structure. The solution parameters intervening in the SMT degradation kinetics were investigated in detail as well as the properties of the photocatalyst surface. This study provides the first evidence for ZnO/Cu_xO iso-energetic electron transfer between Cu_xO to ZnO, leading to the degradation of SMT. There are some

initial reports about ZnO/Cu$_x$O nanowires photoelectrochemical-mediated H$_2$ production activated by visible light due to the extended visible light absorption spectrum of Cu$_x$O. This is an advance with respect to ZnO-mediated generation of H$_2$ that proceeds with a low efficiency using a costly UV-light. Some preliminary studies reported on ZnO/Cu$_x$O nanowires as humidity and pH sensors, but no commercial devices have been developed and commercialized until now. Further work to exploit the practical potential of the ZnO/CuO nanowires is warranted at this time. Several studies in scientific journals have reported on ZnO/Cu$_x$O nanowires addressing the degradation of cationic and anionic dyes. However, no flow reactors leading to photoelectrochemical dye degradation-mediated ZnO/Cu$_x$O nanowires have been reported so far.

Supplementary Materials: The following are available online at http://www.mdpi.com/2073-4344/9/11/916/s1, Figure S1: Effect of SMT-concentration on the degradation kinetics under (a) simulated solar light and (b) visible light irradiation. Solution parameters: [catalyst]=500 mg/L, initial pH 7.0, solar light intensity 50.1 mW/cm2 and visible light intensity 38.9 mW/cm2, Figure S2: Effect of ZnO/Cux=1.25O concentration on the SMT-degradation kinetics under (a) simulated solar light and (b) visible light irradiation. Solution parameters: [SMT]=2.5 mg/L, initial pH 7.0, solar light intensity 50.1 mW/cm2 and visible light intensity 38.9 mW/cm2, Figure S3: HPLC spectra of 2.5 mg/L sulfamethazine in the presence of (a) no NaN3, (b) 0.01 mM NaN3, (c) 0.1 mM NaN3 and (d) 0.5 mM NaN3. Note that the peak areas of (a), (b), (c) and (d) are 122.7, 131.5, 163.0 and 184.1, Figure S4: Effect of solution pH on the SMT-degradation kinetics by ZnO/Cux=1.25O under (a) simulated solar light and (b) visible light irradiation. Solution parameters: [catalyst]=500 mg/L, [SMT]=2.5 mg/L, solar light intensity 50.1 mW/cm2 and visible light intensity 38.9 mW/cm2, Table S1: The pH value of SMT solution after photodegradation by ZnO/Cux=1.25O under simulated solar light for a certain time, Table S2: The pH value of SMT solution after photodegradation by ZnO/Cux=1.25O under visible light for a certain time.

Author Contributions: Conceptualization: S.R. and J.K.; Methodology: S.R. and J.Y.; Investigation and Experimental: J.Y.; Resources: C.P. and T.W.; Supervision: S.R.; Writing—original draft preparation: J.K. and S.R.; Final draft: S.R.

Conflicts of Interest: The authors declare no conflict of interest.

References

1. Tolls, J. Sorption of veterinary pharmaceuticals in soils: A review. *Environ. Sci. Technol.* **2001**, *35*, 3397–3406. [CrossRef] [PubMed]

2. Poirier, A.; Doerge, R.; Gaylor, W.; Miller, A.; Lorentzen, J.; Casciano, A.; Kadlubar, F.; Schwetz, A. An FDA Review of Sulfamethazine Toxicity. *Regul. Toxicol. Pharmacol.* **1999**, *30*, 217–222. [CrossRef] [PubMed]

3. De Liguoro, M.; Fioretto, B.; Poltronieri, C.; Gallina, G. The toxicity of sulfamethazine to Daphnia magna and its additivity to other veterinary sulfonamides and trimethoprim. *Chemosphere* **2009**, *75*, 1519–1524. [CrossRef] [PubMed]

4. Teixidó, M.; Pignatello, J.; Beltrán, L.; Granados, M.; Peccia, J. Speciation of the ionizable antibiotic sulfamethazine on black carbon (biochar). *Environ. Sci. Technol.* **2011**, *45*, 10020–10027. [CrossRef] [PubMed]

5. Wegst-Uhrich, R.; Navarro, A.; Zimmerman, L.; Aga, S. Assessing antibiotic sorption in soil: A literature review and new case studies on sulfonamides and macrolides. *Chem. Cent. J.* **2014**, *8*, 5–20. [CrossRef]

6. Ingerslev, F.; Halling-Sørensen, B. Biodegradability properties of sulfonamides in activated sludge. *Environ. Toxicol. Chem.* **2000**, *19*, 2467–2473. [CrossRef]

7. Göbel, A.; Thomsen, A.; McArdell, S.; Alder, C.; Giger, W.; Theiß, N.; Löffler, D.; Ternes, D.A. Extraction and determination of sulfonamides, macrolides, and trimethoprim in sewage sludge. *J. Chromatogr. A* **2005**, *1085*, 179–189. [CrossRef]

8. Dolliver, H.; Kumar, K.; Gupta, S. Sulfamethazine uptake by plants from manure-amended soil. *J. Eviron. Qual.* **2007**, *36*, 1224–1230. [CrossRef]

9. Kemper, N. Veterinary antibiotics in the aquatic and terrestrial environment. *Ecol. Ind.* **2008**, *8*, 1–13. [CrossRef]

10. Boxall, B.; Johnson, P.; Smith, J.; Sinclair, J.; Stutt, E.; Levy, S. Uptake of veterinary medicines from soils into plants. *J. Agric. Food Chem.* **2006**, *54*, 2288–2297. [CrossRef]

11. Wan, Z.; Wang, J. Degradation of sulfamethazine using Fe_3O_4-Mn_3O_4/reduced graphene oxide hybrid as Fenton-like catalyst. *J. Hazard. Mater.* **2017**, *324*, 653–664. [CrossRef] [PubMed]

12. Qiang, Z.; Xiaolei, B.; Weiwei, B. MCM-48 modified magnetic mesoporous nanocomposite as an attractive adsorbent for the removal of sulfamethazine from water. *Water Res.* **2013**, *47*, 4107–4114. [CrossRef] [PubMed]

13. Braschi, I.; Blasioli, S.; Gigli, L.; Gessa, E.; Alberti, A.; Martucci, A.J. Removal of sulfonamide antibiotics from water: Evidence of adsorption into an organophilic zeolite Y by its structural modifications. *Hazard. Mater.* **2010**, *178*, 218–225. [CrossRef] [PubMed]

14. Zhang, C.; Lai, C.; Zeng, G.; Huang, D.; Yang, C.; Wang, Y.; Zhou, Y.; Cheng, M. Efficacy of carbonaceous nanocomposites for sorbing ionizable antibiotic sulfamethazine from aqueous solution. *Water Res.* **2016**, *95*, 103–112. [CrossRef] [PubMed]

15. Xu, J.; Sheng, P.; Ma, Y.; Wang, F.; Yu, Q. Roles of extracellular polymeric substances (EPS) in the migration and removal of sulfamethazine in activated sludge system. *Water Res.* **2013**, *47*, 5298–5306. [CrossRef] [PubMed]

16. Topp, E.; Chapman, R.; Devers-Lamrani, M.; Hartmann, A.; Marti, R.; Martin-Laurent, F.; Sabourin, L.; Scott, A.; Sumarah, M.J. Accelerated biodegradation of veterinary antibiotics in agricultural soil following long-term exposure, and isolation of a sulfamethazine-degrading *Microbacterium* sp. *Environ. Qual.* **2014**, *42*, 173–178. [CrossRef]

17. Reis, J.; Reis, C.; Ricken, C.; Kolvenbach, B.; Manaia, M.; Corvini, F.; Nunes, C.J. Biodegradation of sulfamethoxazole and other sulfonamides by Achromobacter denitrificans PR1. *Hazard. Mater.* **2014**, *280*, 741–749. [CrossRef]

18. Zhou, T.; Wu, X.; Zhang, Y.; Li, J.; Lim, T. Synergistic catalytic degradation of antibiotic sulfamethazine in a heterogeneous sonophotolytic goethite/oxalate Fenton-like system. *Appl. Catal. B Environ.* **2013**, *136*, 294–301. [CrossRef]

19. Pérez-Moya, M.; Graells, M.; Castells, G.; Amigó, J.; Ortega, E.; Buhigas, G.; Pérez, M.; Mansilla, H. Characterization of the degradation performance of the sulfamethazine antibiotic by photo-Fenton process. *Water Res.* **2010**, *44*, 2533–2540. [CrossRef]

20. Sopaj, F.; Oturan, N.; Pinson, J.; Podvorica, F.; Oturan, A. Effect of the anode materials on the efficiency of the electro-Fenton process for the mineralization of the antibiotic sulfamethazine. *Appl. Catal. B Environ.* **2016**, *199*, 331–341. [CrossRef]

21. Garoma, T.; Umamaheshwar, K.; Mumper, A. Removal of sulfadiazine, sulfamethizole, sulfamethoxazole, and sulfathiazole from aqueous solution by ozonation. *Chemosphere* **2010**, *79*, 814–820. [CrossRef] [PubMed]

22. Liu, Y.; Wang, J.J. Degradation of sulfamethazine by gamma irradiation in the presence of hydrogen peroxide. *Hazard. Mater.* **2013**, *250*, 99–105. [CrossRef] [PubMed]

23. Guo, C.; Xu, J.; Wang, S.; Zhang, Y.; He, Y.; Li, X. Photodegradation of sulfamethazine in an aqueous solution by a bismuth molybdate photocatalyst. *Catal. Sci. Technol.* **2013**, *3*, 1603–1611. [CrossRef]

24. Zhou, C.; Lai, C.; Xu, P.; Zeng, G.; Huang, D.; Zhang, C.; Cheng, M.; Hu, L.; Wan, J.; Liu, Y.; et al. In Situ Grown AgI/Bi12O17Cl2 Heterojunction Photocatalysts for Visible Light Degradation of Sulfamethazine: Efficiency, Pathway, and Mechanism. *ACS Sustain. Chem. Eng.* **2018**, *6*, 4174–4184. [CrossRef]

25. Kolodziejczak-Radzimska, A.; Jesionowski, T. Zinc oxide—From synthesis to application: A review. *Materials* **2014**, *7*, 2833–2881. [CrossRef] [PubMed]

26. Pelaez, M.; Nolan, N.T.; Pillai, S.C.; Seery, M.K.; Falaras, P.; Kontos, A.G.; Dunlop, P.S.; Hamilton, J.W.; Byrne, J.A.; O'shea, K.; et al. A review on the visible light active titanium dioxide photocatalysts for environmental applications. *Appl. Catal. B* **2012**, *125*, 331–349. [CrossRef]

27. Banerjee, S.; Pillai, S.C.; Falaras, P.; O'Shea, K.; Byrne, J.; Dionysiou, D.J. New insights into the mechanism of visible light photocatalysis. *Phys. Chem. Lett.* **2014**, *5*, 2543–2554. [CrossRef]

28. Etacheri, V.; Di Valentin, C.; Schneider, J.; Bahnemann, D.; Pillai, S.C. Visible-light activation of TiO2 photocatalysts: Advances in theory and experiments. *J. Photochem. Photobiol. C Photochem. Rev.* **2015**, *25*, 1–29. [CrossRef]

29. Nozik, A. Photoelectrochemistry: Applications to solar energy conversion. *Annu. Rev. Phys. Chem.* **1978**, *29*, 189–222. [CrossRef]

30. Mamba, G.; Kiwi, J.; Pulgarin, C.; Sanjines, R.; Giannakis, S.; Rtimi, S. Evidence for the degradation of an emerging pollutant by a mechanism involving iso-energetic charge transfer under visible light. *Appl. Catal. B Environ.* **2018**, *233*, 175–183. [CrossRef]

31. Kung, Y.; Cai, L.; Pan, F.; Shen, W.; Su, H. Photonic Fano Resonance of Multishaped Cu_2O Nanoparticles on ZnO Nanowires Modulating Efficiency of Hydrogen Generation in Water Splitting Cell. *ACS Sustain. Chem. Eng.* **2018**, *6*, 6590–6598. [CrossRef]

32. Yu, J.; Kiwi, J.; Wang, T.; Pulgarin, C.; Rtimi, S. Evidence for a dual mechanism in the TiO_2/CuxO photocatalyst during the degradation of sulfamethazine under solar or visible light: Critical issues. *J. Photochem. Photobiol. A* **2019**, *375*, 270–279. [CrossRef]

33. Niedziolka-Jonsson, J.; Mackowski, S. Plasmonics with Metallic Nanowires. *Materials* **2019**, *12*, 1418–1432.

34. Hou, W.; Cronin, S.B. A review of surface plasmon resonance-enhanced photocatalysis. *Adv. Funct. Mater.* **2013**, *12*, 1612–1619. [CrossRef]

35. Qiu, X.; Miyauchi, M.; Sunada, K.; Minoshima, M.; Liu, M.; Lu, Y.; Li, D.; Shimodaira, Y.; Hosogi, Y.; Kuroda, Y.; et al. Hybrid Cu_xO/TiO_2 nanocomposites as risk-reduction materials in indoor environments. *Acs Nano* **2012**, *6*, 1609–1618. [CrossRef]

36. Wang, H.; Tam, F.; Grady, N.K.; Halas, N.J. Cu nanoshells: Effects of interband transitions on the nanoparticle plasmon resonance. *J. Phys. Chem. B* **2005**, *109*, 18218–18222. [CrossRef]

37. Singhal, S.; Kaur, J.; Namgyal, T.; Sharma, R. Cu-doped ZnO nanoparticles: Synthesis, structural and electrical properties. *Phys. B Condens. Mater* **2012**, *407*, 1223–1229. [CrossRef]

38. Fujishima, A.; Zhang, X.; Tryk, D. TiO_2 photocatalysis and related surface phenomena. *Surf. Sci. Rep.* **2008**, *63*, 515–582. [CrossRef]

39. Vuong, M.; Chinh, D.; Huy, T.; Lee, I. CuO-Decorated ZnO Hierarchical Nanostructures as Efficient and Established Sensing Materials for H_2S Gas Sensors. *Sci. Rep.* **2016**, *6*, 26736.

40. Ahmad, R.; Tripathy, N.; Ahn, S.; Bhat, S.; Mahmoudi, T.; Wang, Y.; Yoo, Y.; Kwon, W.; Yang, H.; Hahn, B.Y. Highly Efficient Non-Enzymatic Glucose Sensor Based on CuO Modified Vertically-Grown ZnO Nanorods on Electrode. *Sci. Rep.* **2017**, *7*, 5715–5718. [CrossRef]

41. Skårman, B.; Grandjean, D.; Benfield, E.; Hinz, A.; Andersson, A.; Wallenberg, R.J. Carbon monoxide oxidation on nanostructured $CuOx$/CeO_2 composite particles characterized by HREM, XPS, XAS, and high-energy diffraction. *Catalysis* **2002**, *211*, 119–133. [CrossRef]

42. Kraeutler, B.; Bard, A.J. Heterogeneous photocatalytic synthesis of methane from acetic acid-new Kolbe reaction pathway. *Am. Chem. Soc.* **1978**, *100*, 2239–2240. [CrossRef]

43. Fan, Y.; Ji, Y.; Kong, D.; Lu, J.; Zhou, Q. Kinetic and mechanistic investigations of the degradation of sulfamethazine in heat-activated persulfate oxidation process. *J. Hazard. Mater.* **2015**, *300*, 39–47. [CrossRef] [PubMed]

44. Cairns, D. *Essentials of Pharmaceutical Chemistry*, 3rd ed.; Pharmaceutical Press: London, UK; Chicago, IL, USA, 2008; p. 69.

45. Fernandez, J.; Nadtochenko, V.; Kiwi, J. Photobleaching of Orange II within seconds using the oxone/Co 2+ reagent through Fenton-like chemistry. *Chem. Commum.* **2003**, *18*, 2382–2383. [CrossRef] [PubMed]

46. Parks, G. The isoelectric points of solid oxides, solid hydroxides, and aqueous hydroxo complex systems. *Chem. Rev.* **1965**, *65*, 177–198. [CrossRef]

47. Tacic, A.; Nicolic, V.; Nicolic, L.; Savic, I. Antimicrobial sulfonamide drugs. *Adv. Technol.* **2017**, *6*, 58–71. [CrossRef]

48. Hu, J.; Liu, P.; Chen, L. Comparison of surface plasmon resonance responses to dry/wet air for Ag, Cu, and Au/SiO_2. *Appl. Opt.* **2012**, *51*, 1357–1360. [CrossRef]

49. Khanehzaeri, H.; Ahmad, M.; Shameli, K.; Ajdari, Z. Synthesis and characterization of Cu@ Cu_2O core shell nanoparticles prepared in seaweed Kappaphycus alvarezii Media. *J. Electrochem. Sci.* **2014**, *9*, 8189–8198.

50. Liu, X.; Swihart, M. Heavily-doped colloidal semiconductor and metal oxide nanocrystals: An emerging new class of plasmonic nanomaterials. *Chem. Soc. Rev.* **2014**, *43*, 3908–3920. [CrossRef]

51. Mendelsberg, J.; McBride, M.; Duong, T.; Bailey, M.; Llordes, A.; Milliron, J.; Helms, A. Dispersible Plasmonic Doped Metal Oxide Nanocrystal Sensors that Optically Track Redox Reactions in Aqueous Media with Single-Electron Sensitivity. *Adv. Opt. Mater.* **2015**, *3*, 1293–1300. [CrossRef]

52. Sulzberger, B.; Canonica, S.; Egli, T.; Giger, W.; Klausen, J.; von Gunten, U. Oxidative transformations of contaminants in natural and in technical systems. *Chimia* **1997**, *51*, 900–907.

53. Wardman, P.J. Reduction potentials of one-electron couples involving free radicals in aqueous solution. *Phys. Chem. Ref. Data* **1989**, *18*, 1637–1755. [CrossRef]

54. Mills, A. An overview of the methylene blue ISO test for assessing the activities of photocatalytic films. *Appl. Catal. B* **2012**, *128*, 144–149. [CrossRef]

55. Jing, L.; Zhou, W.; Tian, G.; Fu, H. Surface tuning for oxide-based nanomaterials as efficient photocatalysts. *Chem. Soc. Rev.* **2013**, *42*, 9509–9549. [CrossRef]

56. Yu, J.; Kiwi, J.; Zivkovic, I.; Rønnow, H.M.; Wang, T.; Rtimi, S. Quantification of the local magnetized nanotube domains accelerating the photocatalytic removal of the emerging pollutant tetracycline. *Appl. Cat. B Environm.* **2019**, *248*, 450–458. [CrossRef]

57. Tamaekong, N.; Phanichphant, S.; Wisitsoraat, A.; Liewhiran, C. Core/Shell of p-Cu_xO/n-ZnO Nanowire Arrays for H_2S Gas Sensor. *Solid. State Phenom.* **2018**, *283*, 7–15. [CrossRef]

58. Elfadill, N.; hashim, M.; Saron, K.; Charour, K.; Qaeed, M.; Bououdina, M. Ultraviolet–visible photo-response of p-Cu2O/n-ZnO heterojunction prepared on flexible (PET) substrate. *Mater. Chem. Phys.* **2015**, *156*, 54–60. [CrossRef]

59. Maccato, C.; Berreca, D.; Carraro, G.; Gasparotto, A.; Gombac, V.; Fornasiero, P. CuO_x-TiO_2 Photocatalysts for H_2 Production from Ethanol and Glycerol Solutions. *Surf. Coat. Technol.* **2013**, *230*, 219–222. [CrossRef]

60. Zhang, Y.; Stefanakos, M.R.E.; Goswami, D. Synthesis, characterization, and applications of ZnO nanowires. *J. Nanomater.* **2012**, *2012*, 624520. [CrossRef]

61. Shirley, D.A. High-resolution X-ray photoemission spectrum of the valence bands of gold. *Phys. Rev. B* **1972**, *5*, 4709–4714. [CrossRef]